

## Wind flow and its interaction with a mobile solar PV system mounted on a trailer

Item Type	Journal article
Authors	Eslami Majd, Alireza;Adebayo, David Shina;Tchuenbou-Magaia, Fideline Laure;Willetts, James;Nwosu, Dave;Matthews, Zachary;Ekere, Nduka Nnamdi
Citation	Eslami Majd A, Adebayo DS, Tchuenbou-Magaia F, Willetts J, Nwosu D, Matthews Z, Ekere NN. Wind Flow and Its Interaction with a Mobile Solar PV System Mounted on a Trailer. Sustainability. 2024; 16(5):2038. <a href="https://doi.org/10.3390/su16052038">https://doi.org/10.3390/su16052038</a>
DOI	<a href="https://doi.org/10.3390/su16052038">10.3390/su16052038</a>
Publisher	MDPI
Journal	Sustainability
Download date	2026-06-18 14:34:09
License	<a href="https://creativecommons.org/licenses/by/4.0/">https://creativecommons.org/licenses/by/4.0/</a>
Link to Item	<a href="http://hdl.handle.net/2436/625457">http://hdl.handle.net/2436/625457</a>

Article

# Wind Flow and Its Interaction with a Mobile Solar PV System Mounted on a Trailer

Alireza Eslami Majd <sup>1,\*</sup>, David S. Adebayo <sup>1,†</sup>, Fideline Tchuenbou-Magaia <sup>1</sup>, James Willetts <sup>2</sup>, Dave Nwosu <sup>3</sup>, Zackery Matthews <sup>4</sup> and Nduka Nnamdi Ekere <sup>5</sup>

<sup>1</sup> Energy and Green Technology Research Group, Centre for Engineering Innovation and Research, University of Wolverhampton, Telford Innovation Campus, Telford TF2 9NT, UK; d.adebayo@wlv.ac.uk (D.S.A.); f.tchuenbou-magaia@wlv.ac.uk (F.T.-M.)

<sup>2</sup> AceOn Group, Telford TF3 3BJ, UK

<sup>3</sup> Nevadic Limited, R24B Romanus Orji Street, Southern View Estate, Lekki 023401, Lagos, Nigeria

<sup>4</sup> DZP Technologies Limited, Cambridge CB4 2HY, UK

<sup>5</sup> Faculty of Engineering and Technology, Liverpool John Moores University, Liverpool L3 3AF, UK

\* Correspondence: a.e.majd@wlv.ac.uk

† Current address: School of Engineering and Technology, College of Engineering and Physical Sciences, Aston University, Aston Triangle, Birmingham B4 7ET, UK.

**Abstract:** Efficient implementation of clean energy technologies is paramount, with mobile solar PV systems on trailers (MSPTs) emerging as pivotal solutions, particularly in regions with limited power grid access. This endeavour is vital for meeting escalating electricity demands and aligning with the UN Sustainable Development Goal (SDG), aimed at ensuring dependable and sustainable energy provision in developing countries. This study investigates the aerodynamic behaviour of a designed MSPT using numerical simulation and experimental methods, thereby offering optimization potential for MSPT design and enhancing overall performance and reliability. Specifically, the study focuses on the effects of wind velocity and tilt angles on the drag and lift forces, as well as drag and lift coefficients on the panel used in the MSPT system. The overall wind force on the entire MSPT, including nine large solar PV panels, is scrutinised, considering combined wind flow and system geometry effects. The numerical investigations were conducted using ANSYS-Fluent software (version 2022/R2) and experimental testing was performed within the C15-10 Wind Tunnel, utilizing scaled-down models to validate the accuracy of the simulation. The findings from the numerical investigations showed an increased turbulence caused by gaps between panels, resulting in almost 62% higher suction flow velocity and 22% higher suction pressure compared to a single panel. Drag and lift forces on the entire MSPT were approximately 6.7 and 7.8 times greater than those on a single panel with the same 30-degree tilt angle, respectively. The findings revealed that scaling forces on a single panel is insufficient for accurately predicting the aerodynamic forces on the entire MSPT. The insights and the knowledge from this study pave the way for further improvements in mobile solar PV technology.

**Keywords:** mobile solar PV system; aerodynamic; Computational Fluid Dynamics (CFD); wind effects; Sustainable Development Goal (SDG)



**Citation:** Eslami Majd, A.; Adebayo, D.S.; Tchuenbou-Magaia, F.; Willetts, J.; Nwosu, D.; Matthews, Z.; Ekere, N.N. Wind Flow and Its Interaction with a Mobile Solar PV System Mounted on a Trailer. *Sustainability* **2024**, *16*, 2038. <https://doi.org/10.3390/su16052038>

Academic Editors: Fu Gu, Jingxiang Lv and Shun Jia

Received: 26 December 2023

Revised: 11 February 2024

Accepted: 20 February 2024

Published: 29 February 2024



**Copyright:** © 2024 by the authors. Licensee MDPI, Basel, Switzerland. This article is an open access article distributed under the terms and conditions of the Creative Commons Attribution (CC BY) license (<https://creativecommons.org/licenses/by/4.0/>).

## 1. Introduction

The need for sustainable development, reduction in energy-related greenhouse gas emissions, and the desire to attain carbon-neutral economy have been major contributing factors in the drive to shift from fossil-based systems of energy production and consumption towards renewable and clean energy sources. Photovoltaic (PV) harvesting energy systems constitute one of the major technologies which could contribute to meeting the UN Sustainable Development Goal (SDG) on ensuring reliable and sustainable energy supply through effective sun energy harvesting to generate electricity while minimizing adverse

environmental impacts [1]. This encompasses the introduction of the solar PV system as a key renewable energy source, feasible for electricity generation at convincing costs per kilowatt in diverse global regions [2,3].

Mobile solar PV systems play a crucial role in regions where access to the power grid is limited or unreliable [4]. These systems provide a sustainable and independent source of energy, particularly in remote areas or during emergencies such as in healthcare buildings. The mobility of solar PV systems allows them to be easily deployed and relocated as needed, making them suitable for various applications such as disaster relief efforts, outdoor events, and mobile installations, including recreational vehicles and boats. Advancements in battery storage technology have improved their effectiveness by enabling energy storage for use during non-sunlight hours. This ensures a consistent power supply even in off-grid locations. Despite the several advantages of the mobile solar PV systems, one of the challenging problems that needs to be addressed is ensuring the structural integrity of solar panels to withstand wind loads in various circumstances. Solving or reducing this challenge will have significant impacts on the deployment of the system.

## 2. Literature Review

The aerodynamics of solar panels are categorised into roof-mounted panels and ground-mounted, depending on the wind conditions and turbulence intensity [5]. The most popular method of installation is roof-mounted solar systems for generating clean and renewable energy. A solar PV system erected on a roof can be installed on flat or sloping roofs, including metal composite roofs or rubber materials. When installed on residential, commercial, or industrial buildings, they can provide significant cost savings on electricity bills and help to reduce greenhouse gas emissions [6,7]. Roof-mounted panels are influenced by surrounding walls and building edges, causing airflow separation and vortex generation, which may lead to a high-pressure zone on the roof [8]. The loads on the panels are determined by their inclination angle, affected by different factors including wind direction, panel position, and building height [9,10]. A ground-mounted solar system, on the other hand, is a free-standing solar system that is mounted on the ground. These solar systems are installed with a metal frame or a single pole. The same type of solar panels is used in ground-mounted solar PV systems as in rooftop systems, but they are installed differently. Ground-mounted solar panels, located within the boundary layer, require precise array configuration, wind direction, and wind speed and turbulence definitions for accurate load calculations [11,12].

The analytical investigation aims to utilise aerodynamic formulations to determine the forces experienced by the panels. The lift force represents the component of the aerodynamic force that acts perpendicular to the airflow and is mathematically described by Equation (1). Likewise, the drag force corresponds to the component of the aerodynamic force that acts tangentially to the airflow and can be expressed by Equation (2).

$$F_L = \frac{1}{2} A \rho C_L V^2 \quad (1)$$

$$F_D = \frac{1}{2} A \rho C_D V^2 \quad (2)$$

where  $F_L$  and  $F_D$  are lift and drag forces (N), respectively.  $A$  is the area ( $\text{m}^2$ ) of the panel subjected to the air flow,  $\rho$  is the mass density ( $\text{kg}/\text{m}^3$ ) of the air flow, and  $V$  is the velocity ( $\text{m}/\text{s}$ ) of wind relative to the panel.  $C_L$  and  $C_D$  are the lift and drag coefficients, respectively.

Obtaining accurate values for  $C_L$  and  $C_D$  is crucial when calculating the aerodynamic forces on the panels analytically. These coefficients need to be determined specifically for each panel size and tilting position. The most reliable method for determining these coefficients is using experimental tests. Experimental tests allow the determination of aerodynamic forces, drag coefficient, lift coefficient, and other parameters on physical models placed in a wind tunnel under controlled conditions. On the other hand, CFD

simulations utilise a numerical method to simulate airflow around the panels and estimate the resulting forces, lift, and drag coefficients.

For industrial applications, it is preferable to adhere to standard codes such as the International Building Code (IBC) and American Society of Civil Engineers (ASCE) standard ASCE 7, particularly for the roof-mounted panels. The International Building Code (IBC) serves as a suitable standard for assessing wind loads on structures, including solar panels [13]. Additionally, ASCE 7 provides comprehensive guidelines for determining wind loads and their impacts on solar panel installations [14]. These standards offer insights into wind load requirements based on factors such as building height, location, wind speed, and exposure. However, for certain structures like mobile solar PV systems mounted on trailers (MPSTs), the availability of specific standards and codes may be limited or not directly applicable. This can pose a challenge when it comes to parameter selection in ensuring the structural integrity and resilience of such systems in the face of wind loads.

In cases where standard codes may not exist, it becomes crucial to adopt a rigorous and comprehensive approach to address wind load concerns. This typically involves leveraging engineering principles, expertise, and best practices to design and implement solar PV module systems that can withstand various wind conditions. For such situations, there are two primary approaches that can be employed for predicting wind load effects on solar panels. The first approach involves placing a scaled model of the solar panel in a wind tunnel, where loads are determined using measured parameters on the model [15–17]. The second approach utilises numerical simulation, which has significantly advanced due to the progress made in the information technology (IT) sector. Wind tunnel testing involves constructing a scaled model of the solar panel system and subjecting it to controlled wind conditions [18]. On the other hand, numerical simulations utilise computational models and algorithms to simulate wind flow and its interaction with the solar PV power system [19,20]. Both approaches complement each other, as the results obtained from the wind tunnel testing helps in the validation of the numerical approach. The latter helps with design optimisation and can provide a comprehensive assessment of wind load effects on solar panels.

This paper presents a study that employs both experimental and numerical techniques to investigate the behaviour of the solar PV panels used in the designed MSPT. It focuses on analysing the lift and drag forces exerted on the panels by varying wind velocity, including velocity and direction. The study also evaluates the impacts of wind on the solar PV panels used in the system, considering different panel tilt angles. The Computational Fluid Dynamics (CFD) technique was utilised for the comprehensive investigation and analysis, while the experimental testing was conducted using a scaled-down panel sample with a ratio of 1:15.

### 3. Methodology

The methodology used in this study was both numerical and experimental. The numerical simulations (using ANSYS-Fluent 2022/R2 software) were conducted on the solar PV panels as well as the entire MSPT. This helped to determine the magnitude and impact of the wind force on the system with different tilt angles and wind velocities. The experimental tests, on the other hand, were used to validate the results obtained from the numerical estimation.

#### 3.1. Experiments

The experimental tests on the panel sample (scaled 1:15) were conducted using an open circuit wind tunnel. The equipment used was the C15-10 subsonic wind tunnel with an incorporated IFD7 interface, which provides connection to a PC on which the software for controlling the experiment is installed. The software interface helps with sensor output logging and controlling the fan speed, as well as performing any required calculations for each test. The wind tunnel has a square test section with nominal dimensions of 150 mm × 150 mm and 800 mm in length. The base of the wind tunnel's working section

is removable to allow for the insertion of large or complex models when required. The tunnel is designed with an inlet flow straightener and contraction ratio (9.4:1) to give well developed air flow through the working section. Air is drawn through the working section by a variable speed fan at the discharge end of the tunnel, providing up to 34 m/s air velocity. To prevent personnel and objects from coming into contact with the rotating blades, the fan is equipped with a protective grill on the outside.

For this study, the solar panel model was mounted through a circular hatch using quick release clamps (120 mm diameter) in the front wall of the working section. The circular hatch was incorporated with an angular scale, allowing the model to be manually rotated to the desired angle. The transparent working section provided a unique opportunity for flow visualisation around the model.

During the experiment, the fan speed of the wind tunnel was adjusted and kept at a constant speed of 10 m/s, while the angle of attack was increased stepwise from 0 to 35 degrees. The choice of this initial speed was based on the average annual wind speed in the sub-Saharan region, particularly in Nigeria (typically ranging from 2 m/s to 9.5 m/s), where the MSPT is designed to operate. When the desired angle of attack and the velocity have been set, the sensor readings were logged by selecting the start icon on the PC. The fan speed, pressure, lift coefficient, drag coefficient, as well as other parameters were automatically recorded through the software interface in an Excel sheet on the PC for each test. The interfaced computer system was used to record and transfer test data, ensuring precision and reliability throughout the experimental procedures. The experimental results were used to determine the amounts of lift and drag force of wind on the panel sample. Figure 1 depicts a view of the solar PV panel sample installed in the wind tunnel test section.



**Figure 1.** Solar PV panel sample examined in the wind tunnel.

### 3.2. Numerical Simulation

The numerical aerodynamic simulation aids in comprehending the interaction between fluids and solid objects, encompassing both the movement of solid objects through the fluid and the response of static structures to moving fluid (air (wind) in this case). It plays a crucial role in various industries, including aviation, automotive, solar PV arrays, wind energy, and sports equipment design. The computational approach emerges as a cost-effective alternative, circumventing the need for resource-intensive investigations like wind tunnel tests. The numerical simulations have been conducted in this study to determine the associated lift and drag forces based on the experimental test conditions. Comparing the results from the simulation with those from the experiment assisted in validating the simulation set-up for the study involving the full-size panel and entire MSPT.

The critical principles for aerodynamic numerical simulations involve judicious considerations of computational domain, flow conditions, geometrical models, boundary conditions, computational schemes, and domain discretisation. These key fundamental

principles are meticulously discussed in the subsequent subsections, providing a comprehensive understanding of the numerical analysis employed in this study.

### 3.2.1. Computation Domain and Flow Conditions

#### Geometrical Models

A prototype of the MSPT was constructed and affixed to a trailer, as depicted in Figure 2. The MSPT configuration comprises nine panels, featuring six panels (positioned at the top and bottom) tilted at 30 degrees, while the three panels in the middle remain without tilt. The individual solar PV panels employed in the MSPT measure 2.14 m in width and 1.08 m in length. Furthermore, upon unfolding the MSPT with a 30-degree tilt angle, the panels unveil substantial dimensions: a length of 6.61 m, a breadth of 3.45 m, and a height of 1.19 m.



**Figure 2.** Unfolded state of the MSPT with six panels (top and bottom) tilted at 30 degrees.

#### Wind Load

The velocity of 10 m/s was selected, as the MSPT is designed for operating in the sub-Saharan region, particularly in Nigeria, where the average annual wind speeds typically range from 2 m/s to 9.5 m/s [21,22].

#### Boundary Conditions

Figure 3 depicts a 3D representation of the CFD model for the scaled solar panel sample (tilt angle,  $\alpha = 30$  degrees) simulated using ANSYS Fluent 2022 R2. Appropriate boundary conditions were applied with a symmetry boundary condition at the mid-section of the panels, as illustrated in Figure 3, to simplify the analysis. The panels at different tilting angles ( $-35$  to  $35$  degrees) were subjected to a constant wind velocity of 10 m/s. Table 1 provides information on the dimensions of the panel models and the corresponding domain used in the present simulation, including the full-size panel used in the MSPT, scaled panel sample, and panel from the literature [23].

**Table 1.** Model size of the panel (tilted at 30 degrees) and the domain for the present simulations.

	$W_p$	$L_p$	$L_b$	$L_f$	H	B	Unit
Scaled panel sample (scaled 1:15)	72	145	400	200	150	150	
Full-size panel used in the MSPT	1080	2140	4320	2160	1620	2140	mm
Panel from Lit. [23]	699	349	2794	1397	1034	524	

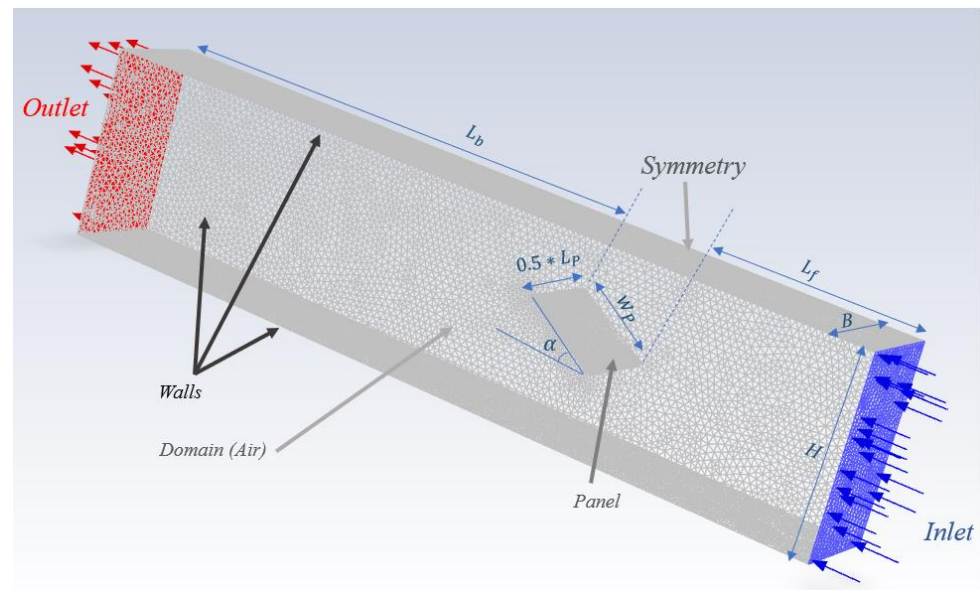


**Figure 3.** 3D view of the CFD model (showing the boundary conditions and the meshing system) used to simulate the panel sample examined in the wind tunnel.

### 3.2.2. Numerical Model Computational Scheme

All the CFD simulations in this current study assume an isothermal, viscous, and incompressible (constant density) fluid. The incompressible Reynolds Averaged Navier Stokes (RANS) equations for the conservation of mass and momentum represented by Equations (3) and (4), and described in the literature, [24,25] govern this flow. The governing equations and turbulence model for the fluid flow in this study have been solved using the defined model and conditions at a steady state. The governing equations are discretised by a finite volume approach and the pressure-based segregated solver proposed by Chorin (1968) has been used for the numerical integration [26]. In this study, the solution method for the pressure-velocity coupling is coupled scheme with the second-order upwind discretisation scheme for modelling the momentum, turbulent kinetic energy, and turbulent dissipation rate. In addition, the convergence of the solution was monitored through the residuals for the relevant equations. When the value of each residual is between three to four orders of magnitude below its initial value, the solution is said to achieve convergence to an acceptable level. In this study, the solution is taken as converged when the momentum and other equations' residuals reduce to  $10^{-4}$  of their initial value.

$$\frac{\partial \rho}{\partial t} + \nabla \cdot (\rho \mathbf{u}) = 0 \quad (3)$$

$$\rho \frac{\partial \mathbf{u}}{\partial t} + \rho \mathbf{u} \cdot \nabla \mathbf{u} = \nabla p + \mu \nabla^2 \mathbf{u} \quad (4)$$

where,  $\partial \rho / \partial t$  represents the rate of change of density ( $\rho$ ) with respect to time ( $t$ ), and  $\nabla \cdot (\rho \mathbf{u})$  denotes the divergence of the product of density and velocity ( $\rho \mathbf{u}$ ) with respect to spatial coordinates ( $x, y, z$ ), and the velocity vector represented by  $\mathbf{u}$ .  $\partial \mathbf{u} / \partial t$  represents the rate of change of velocity with respect to time ( $t$ ) and  $\nabla p$  denotes the pressure gradient.

In this study, the standard k-epsilon turbulence model available in ANSYS Fluent was employed to model the aerodynamic behaviour of a solar PV panels [27]. The turbulence kinetic energy,  $\kappa$ , and its rate of dissipation,  $\varepsilon$ , are obtained from the transport Equations (5) and (6). The standard k-epsilon model is a widely adopted and robust turbulence model known for accurately representing turbulent flow phenomena. The efficacy of this turbulence model has been highlighted in numerous recent research studies examining the impact of wind load and patterns on solar PV panels and arrays, making it a frequent

choice for conducting numerical simulations in this context [10,28–30]. By solving the transport equations for turbulent kinetic energy ( $k$ ) and the dissipation rate of turbulent kinetic energy ( $\epsilon$ ), the model accurately predicts the flow behaviour. Additionally, the standard k-epsilon model was selected due to its versatility and computational efficiency, making it suitable for the simulation of the aerodynamic effects at varying wind velocities and panel tilting angles.

$$\frac{\partial}{\partial t}(\rho k) + \frac{\partial}{\partial x_i}(\rho k u_i) = \frac{\partial}{\partial x_j} \left[ \left( \mu + \frac{\mu_t}{\sigma_k} \right) \frac{\partial k}{\partial x_j} \right] + G_k + G_b - \rho \epsilon - Y_M + S_k \quad (5)$$

$$\frac{\partial}{\partial t}(\rho \epsilon) + \frac{\partial}{\partial x_i}(\rho \epsilon u_i) = \frac{\partial}{\partial x_j} \left[ \left( \mu + \frac{\mu_t}{\sigma_\epsilon} \right) \frac{\partial \epsilon}{\partial x_j} \right] + C_{1\epsilon} \frac{\epsilon}{k} (G_k + C_{3\epsilon} G_b) - C_{2\epsilon} \rho \frac{\epsilon^2}{k} + S_\epsilon \quad (6)$$

In Equations (5) and (6),

$G_k$  = the turbulence kinetic energy due to the mean velocity gradients.

$G_b$  = the generation turbulence kinetic energy due to buoyancy.

$Y_M$  = the contributing effects of fluctuating dilatation to the overall dissipation rate.

$\alpha_k$  and  $\alpha_\epsilon$  = the turbulent Prandtl numbers for  $k$  and  $\epsilon$ , respectively.

$S_k$  and  $S_\epsilon$  = user-defined source terms.

$$\mu_t = \rho C_\mu \frac{k^2}{\epsilon}, \quad (\text{where } C_\mu = \text{constant})$$

The coefficients value for the k-epsilon model were set as presented in Table 2.

**Table 2.** The coefficients used for the standard k-epsilon model in the present simulation using ANSYS Fluent 2022 R2.

Coefficient	Empirical Constants				Turbulent Prandtl Numbers	
	$C_\mu$	$C_{1\epsilon}$	$C_{2\epsilon}$	$C_{3\epsilon}$	$\sigma_k$	$\sigma_\epsilon$
Value	0.09	1.44	1.92	0–1	1	1.3

### Domain Discretisation

The computational domain for this study was meshed in the ANSYS Fluent workbench. The unstructured tetrahedral mesh of intermediate mesh density was used for this current study, as shown in Figure 3. The mesh was clustered around the panel surface by the size function tool in the ANSYS Fluent workbench [27] to capture the salient features of the flow.

### Mesh Sensitivity

To ensure mesh sensitivity and model accuracy, grid independence tests were conducted for various meshing configurations. Seven different meshes were created by adjusting the number of elements along the panel's edges ( $N_p$ ) and the ratio of the domain wall's mesh size to the panel's edge mesh size,  $R_W$ , as documented in Table 3. For the scaled panel sample tilted at 30 degrees, the number of mesh elements ranges from 224 thousand to 2.7 million.

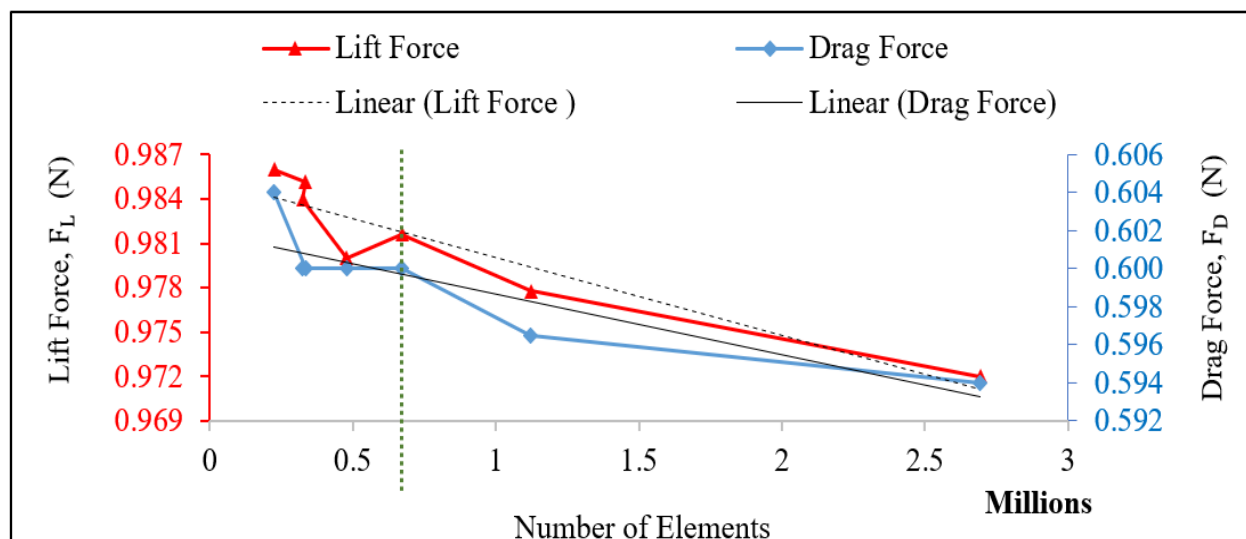
The predictions of the lift and drag forces on the panel were used as monitoring parameters to establish the grid independence of the predictions reported in Table 3. The results of the studied models demonstrated a narrow range of lift and drag forces, with less than a 2% difference in values. The results indicate that the different levels of computational mesh refinement have little impact on the lift and drag forces. This indicates that the numerical scheme is predicting similar values at all the seven levels of mesh refinement and that any further increase in grid density may not noticeably improve the accuracy of the RANS predictions.

**Table 3.** Mesh sensitivity of the simulation of the scaled panel sample tilted at 30 degrees.

Model Number	$N_p$	$R_w$	$N_e$	Lift (N)	Drag (N)
Type 1	100	2.9	2,693,877	0.972	0.594
Type 2	100	4.2	1,123,048	0.978	0.597
Type 3	100	5.6	672,426	<b>0.982</b>	<b>0.600</b>
Type 4	100	6.9	478,405	0.980	0.600
Type 5	100	9.7	325,716	0.984	0.600
Type 6	72	5.6	335,949	0.985	0.600
Type 7	50	5.6	224,593	0.986	0.604
Mean				0.981	0.600
Difference (%)				1.42	1.66
Standard Deviation				0.005	0.003

The computational mesh Type 3, with  $N_p$  of 100,  $R_W$  of 5.6, and  $N_e$  of 672 thousand, shows minimum difference in its corresponding drag and lift forces from the mean values of the forces for all the seven case studies. Mesh Type 3 was chosen for this study as it provides sufficiently grid-independent resolution, given the available computational resources. For the study, the CPU specifications included AMD Ryzen Threadripper PRO 5975WX 32-Cores processor, a 3.60 GHz processor with 64.0 GB (63.8 GB usable) installed RAM, and a 64-bit operating system, x64-based processor for the system type. Additionally, the aerodynamic simulation of the entire MSPT system took an average of 10 h for the iterations to converge.

Figure 4 shows the variation of lift and drag forces with different mesh configurations, displaying linear regression lines that capture the trends of the lift and drag forces as the number of elements in the mesh configuration changes.

**Figure 4.** Variation of lift and drag forces with mesh configuration, showing the linear regression lines for lift force (in red) and drag force (in blue).

### 3.2.3. Numerical Validation

Figure 5 shows the predicted lift and drag forces from the numerical simulation and experimental testing on the scaled solar PV panel sample at a wind velocity of 10 m/s, and varying tilt angles (angle of attack). The results show the drag and lift forces increasing as the angle of attack increases, exhibiting a consistent upward trend. Table 4 shows the results obtained for each of the experiments. Comparing the values of drag and lift forces

and their corresponding coefficients obtained from both the experiments and the simulation of the scaled panel sample, the simulation results in Table 4 show an average error of 8.5% and 4.5% for the lift and the drag forces, respectively, when the tilt angle is over 15 degrees. The results indicate a good agreement between the predicted numerical simulation and experimental data, thereby validating the simulation's accuracy.

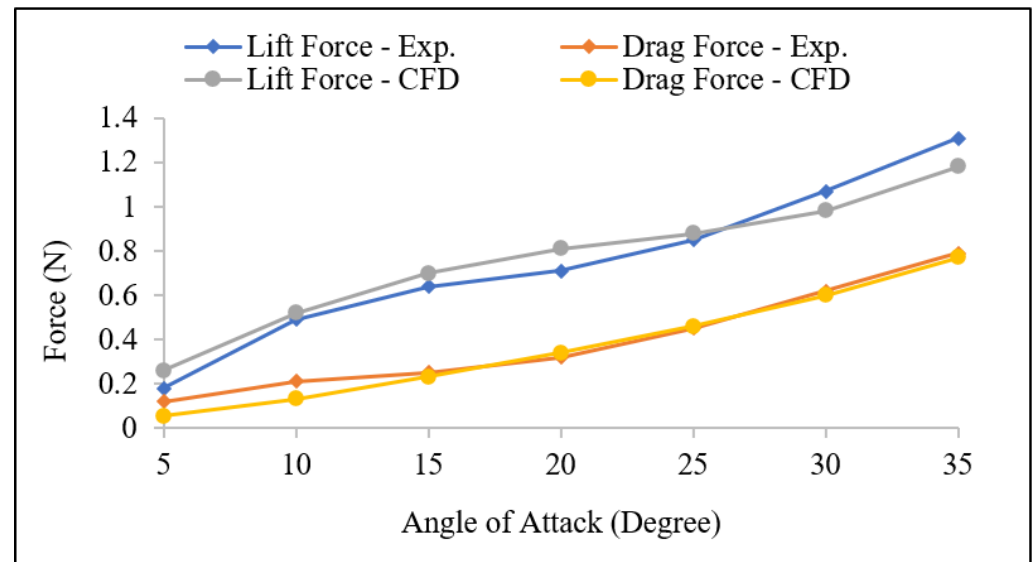


**Figure 5.** Lift and drag forces on solar PV panel sample (scaled 1:15) at 10 m/s wind velocity carried out by experiment and simulation for different tilt angles.

**Table 4.** Lift and drag forces on the scaled panel sample from experiment and CFD simulations.

Angle of Attack (Degree)	Lift (Exp.) (N)	Drag (Exp.) (N)	Lift (CFD) (N)	Drag (CFD) (N)	Lift Error (%)	Drag Error (%)
5	0.18	0.12	0.26	0.055	30.8	54.2
10	0.49	0.21	0.52	0.13	5.8	38.1
15	0.64	0.25	0.7	0.23	8.6	8.0
20	0.71	0.32	0.81	0.34	12.3	5.9
25	0.85	0.45	0.88	0.46	3.4	2.2
30	1.07	0.62	0.98	0.6	8.4	3.2
35	1.31	0.79	1.18	0.77	9.9	2.5
<b>Average Error (%) for angles of attack &gt; 15 degree</b>					<b>8.5</b>	<b>4.5</b>

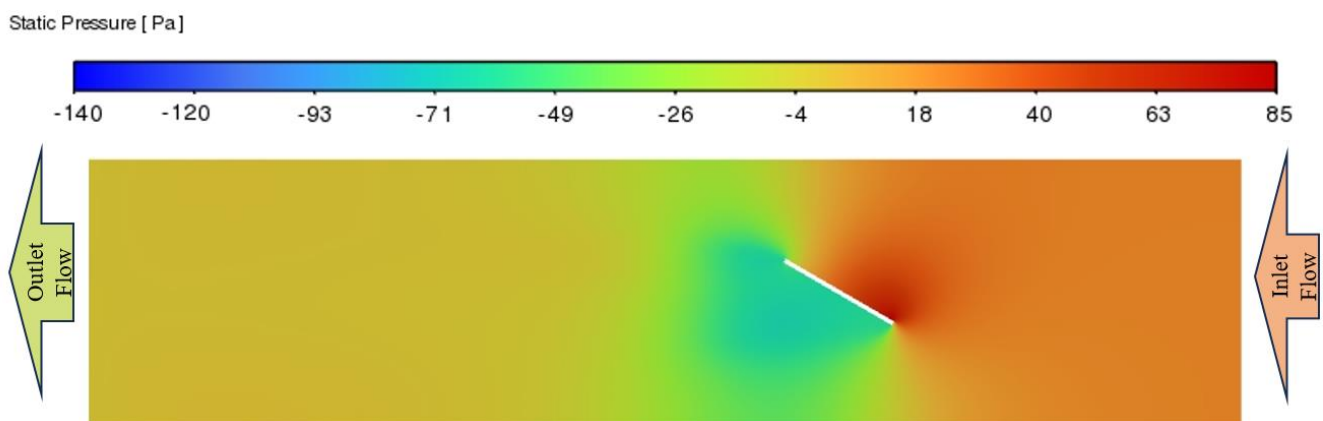
Additionally, the accuracy of the current CFD simulation technique was compared with an unscaled panel described in the literature on both the numerical investigation [23] and the experimental investigation [31], as detailed in the discussion Section 5. The additional analysis aimed to ensure the robustness and reliability of the current study, providing a comprehensive assessment of its performance across different cases. This allowed for the comprehensive aerodynamic performance analysis of the panels under varying wind velocities and tilt angles.

#### 4. Results

This section presents the results of predicted numerical simulations of the flow interaction and behaviour around a single solar panel used in the MSPT and the entire MSPT. The unscaled panel shares a similar aspect ratio of 2 to the panels used in the MSPT, but has different dimensions, as specified in Table 1 (with a width of 699 mm and a length of 340 mm). The drag and lift forces obtained from the current simulation of the tilted panel

at different angles ( $-35$  to  $+35$  degrees) were used to calculate the corresponding lift and drag coefficients using Equations (1) and (2). The air density was taken as  $1.22 \text{ kg/m}^3$ , which is the same as the value used for the CFD simulation, and the wind velocity was set at  $10 \text{ m/s}$ . Furthermore, various parametric studies such as the effects of wind velocity, effect of tilt angle, effect of panel scale factor, and effect of panel aspect ratio on the drag and lift coefficients were investigated and discussed.

Figure 6 displays the static pressure contour at the mid-section of the full-size panel (width:  $1083 \text{ mm}$ , length:  $2140 \text{ mm}$ ) used in the MSPT, tilted at  $30$  degrees, as obtained from the current CFD simulation. As depicted in Figure 6, the leading edge of the panel facing the incoming airflow experienced positive pressure, while the trailing edge of the panel encountered negative pressure, indicating the suction side.



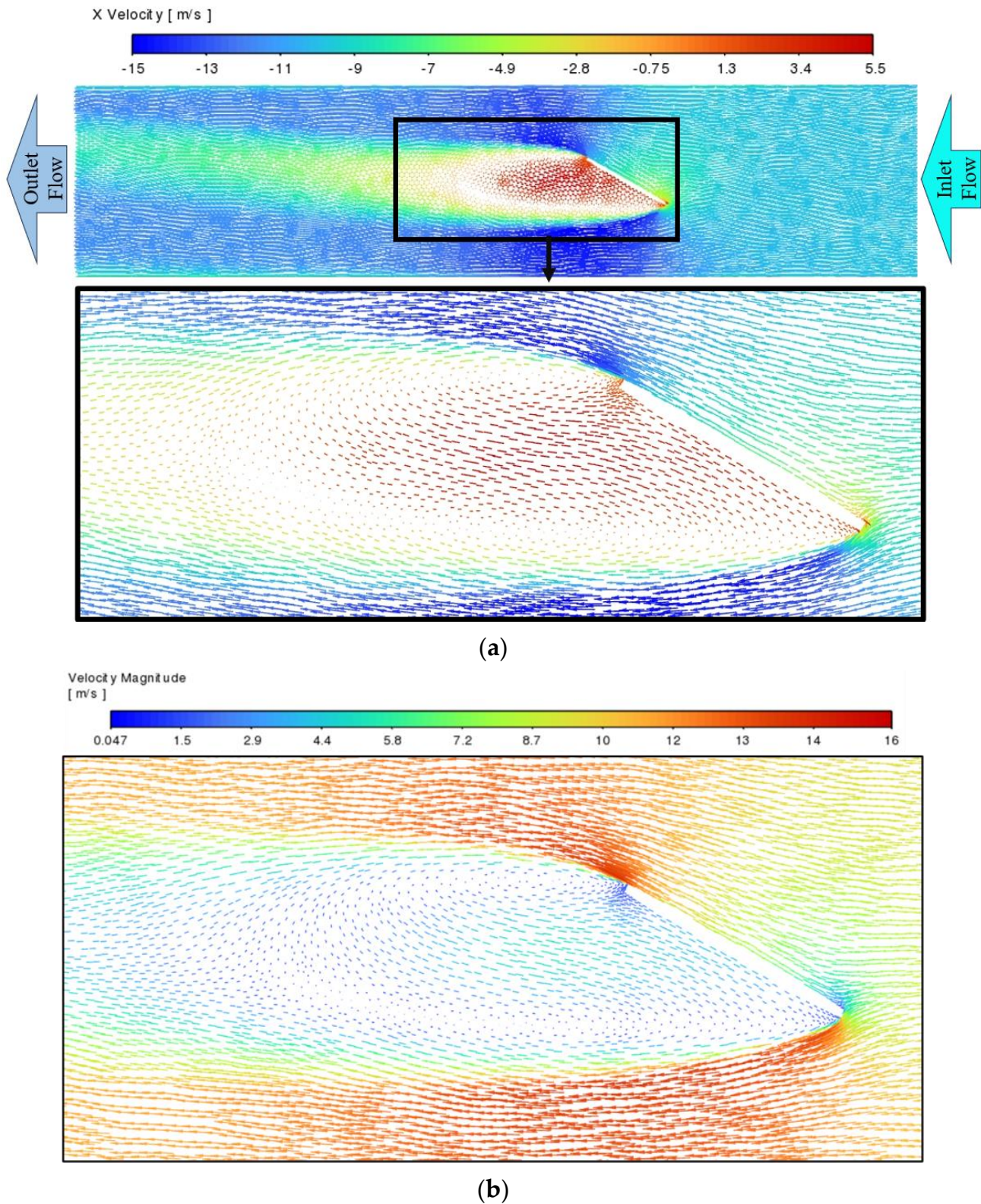
**Figure 6.** Static pressure contour at the mid-section of the full-size solar PV panel used in the MSPT, tilted at  $30$  degrees.

Figure 7a,b depict, respectively, the vector of flow velocity in the  $x$  direction and the vectors of flow velocity magnitude (inlet to outlet), showing the detailed flow behaviour around the panel from the simulation as in Figure 6. Figure 7 illustrates the flow separation occurring at the edges of the panel, accompanied by high turbulence and the generation of vortices at the back of the panel, one near the top edge and the second further away from the bottom edge in the wake region of the panel. The location of the vortices was the low-pressure region behind the panel in Figure 6. The separated flow at the top and bottom edges of the panel resulted in an increase in velocity at the edges, reaching up to  $15 \text{ m/s}$ . Additionally, the vortices at the back of the panel induced a recirculation flow pattern on the opposite side of the inlet flow with an average velocity of  $5.5 \text{ m/s}$ , thus indicating suction effects at the back of the panel.

Figure 8a shows a 3D representation of the flow structure (streamlines of velocity magnitude) around the MPST, which provides further details about the flow structure around the MPST discussed in Figure 7. The result in Figure 8 shows the minimum flow velocity occurring at the back of the panels in the form of recirculating vortex structures, while the maximum flow velocity of  $16 \text{ m/s}$  was observed at the edges of the panel. The features show the solar panels retarding the incoming flow velocity as the flow passes over the panels. The vortex shedding at the back of the panel occurred due to the flow separation around the structures. This recirculation is more visible and pronounced in Figure 8b.

#### 4.1. Effects of Wind Velocity

Figure 9a,b illustrate the variations in drag and lift forces, as well as the corresponding drag and lift coefficients, for the full-size panel used in the MSPT. These variations were observed under different wind velocities and at tilt angles of  $15$  degrees and  $30$  degrees.



**Figure 7.** (a) Vectors of flow velocity in the x direction (inlet to outlet). (b) Vectors of flow velocity magnitude at the mid-section of the full-size solar PV panel used in the MSPT, tilted at 30 degrees.

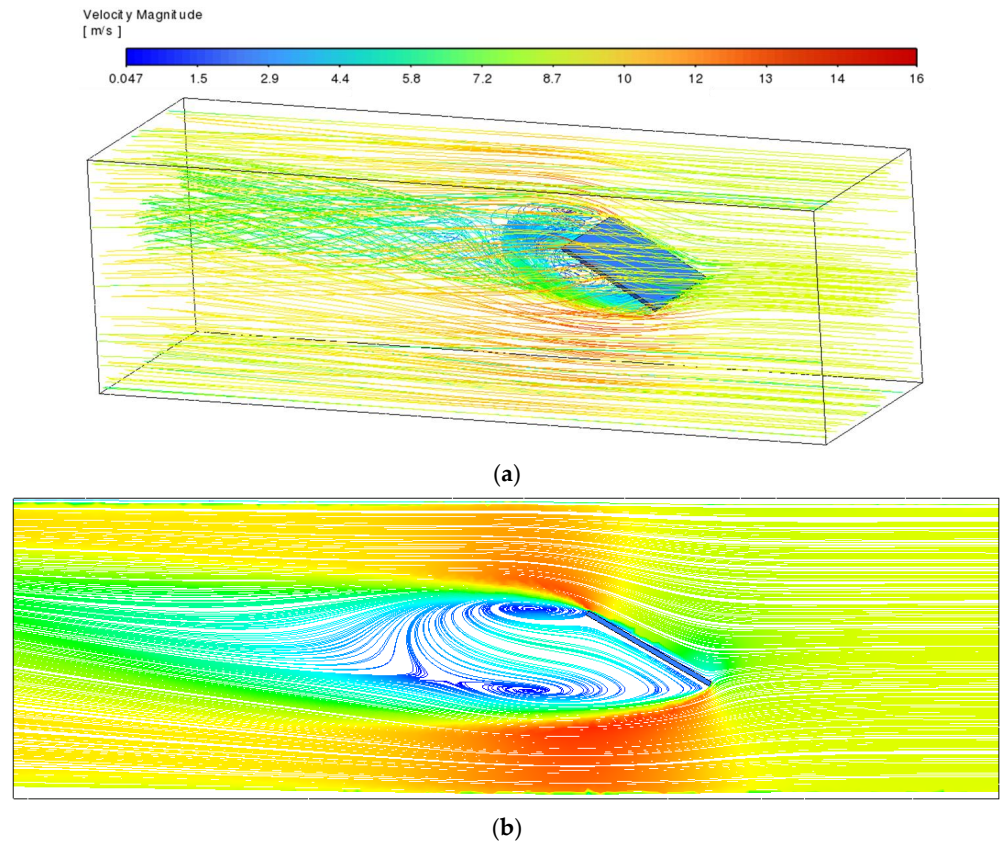


**Figure 8.** (a) 3D representation of flow structure (streamlines of velocity magnitude) around the MSPT (tilted at 30 degrees), (b) 2D flow structure (streamlines of velocity magnitude).

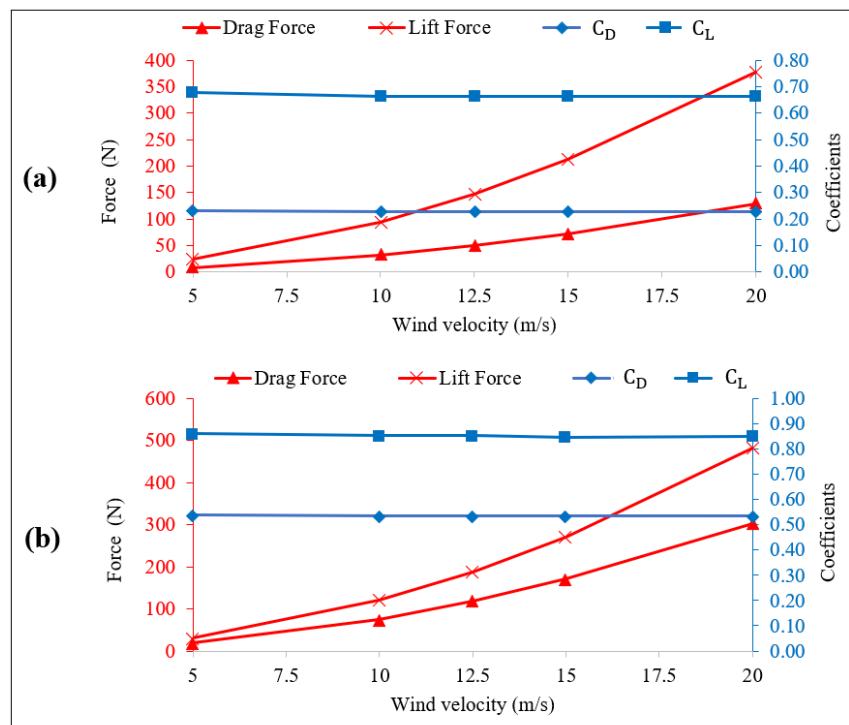


**Figure 9.** Drag and lift forces (in red) and corresponding coefficients,  $C_L$  and  $C_D$  (in blue), on the full-size panel (width: 1083 mm, length: 2140 mm) with different wind velocities: (a) panel tilted at 15 degrees, (b) panel tilted at 30 degrees.

The figures illustrate a consistent trend across different tilt angles, demonstrating that drag and lift forces increase with a quadratic relationship as wind velocities rise. For instance, in Figure 9a, when the panel was tilted at 15 degrees and exposed to a 10 m/s wind, the drag and lift forces measured 32.8 N and 94.2 N, respectively. Doubling the wind velocity to 20 m/s led to an approximate increase to 128 N (drag force) and 377 N (lift force). Notably, the values of  $C_L$  and  $C_D$  for the 15-degree tilted panel remained nearly constant across different wind velocities, with approximate values of 0.23 and 0.66, respectively.

In Figure 9b, with the panel tilted at 30 degrees and subjected to a 10 m/s wind, the drag and lift forces were 76 N and 121 N, respectively. Upon increasing the wind velocity to 20 m/s, the corresponding forces were approximately 303 N (drag force) and 483 N (lift force). Remarkably, the values of  $C_L$  and  $C_D$  for the 30-degree tilted panel remained consistent, unaffected by changes in wind velocity, at 0.53 and 0.85, respectively.

#### 4.2. Effects of Tilt Angle

Figure 10 illustrates the variation of drag and lift forces, as well as the corresponding lift and drag coefficients on the full-size panel with an aspect ratio of two (width: 1083 mm, length: 2140 mm) at different tilt angles ( $-35$  to  $+35$  degrees) and with 10 m/s wind velocity. It is evident from Figure 10 that the trend of drag and lift forces closely follows the trend of the coefficients.

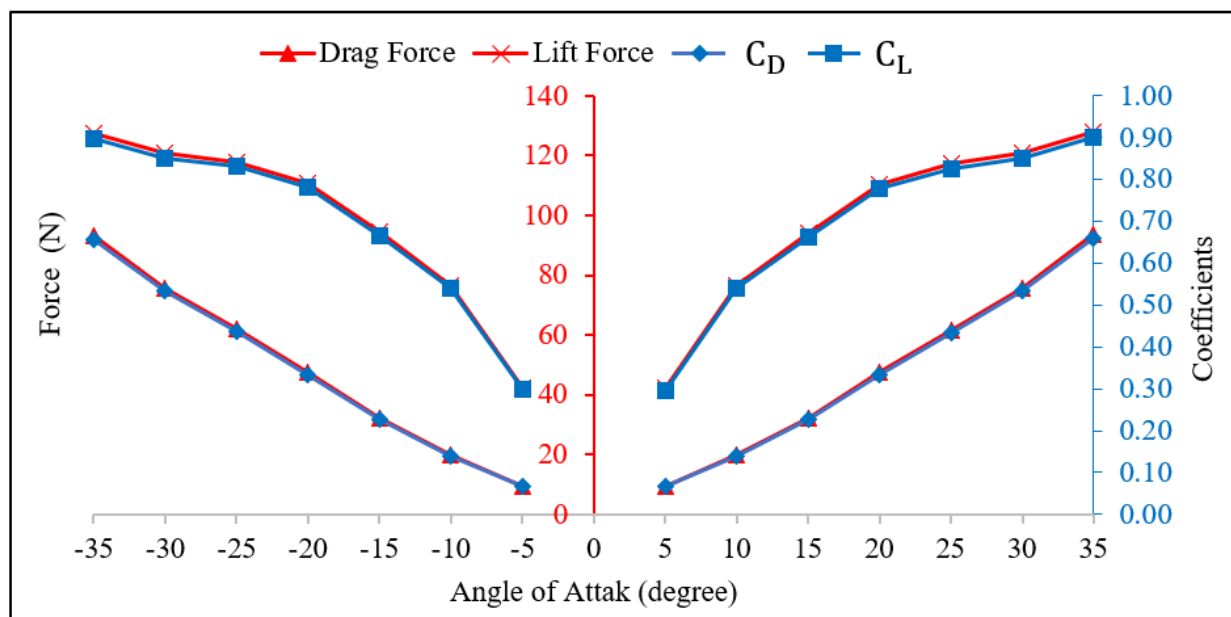


**Figure 10.** Drag and lift forces and coefficients on the full-size panel (width: 1083 mm, length: 2140 mm) at different tilt angles and 10 m/s wind velocity. The primary axis (in red) represents the magnitude of drag and lift forces, while the secondary axis (in blue) shows the corresponding coefficients,  $C_L$  and  $C_D$ .

In agreement with previous results (representing a panel with a different size and aspect ratio, 0.5), it was apparent from Figure 10 that the coefficients  $C_L$  and  $C_D$  were not influenced by the direction of the tilt angle. Also, comparing the results from Figure 10 and Figure 16 in Section 5, similar trends were observed for the values of  $C_L$  and  $C_D$ ; however, different numerical values were obtained. Consequently, this led to further investigation of the effects of panel size (scaling factor) and panel aspect ratio on the aerodynamic coefficients, as discussed in Sections 4.3 and 4.4. This further investigation aimed to deepen knowledge and understanding of the interaction between the different parameters and the resulting aerodynamics of the panels.

#### 4.3. Effect of Panel Scale Factor

To investigate the impact of panel size on the aerodynamic coefficients of solar PV panels, a further CFD study was conducted on panels with various scaling factors. Specifically, simulations were conducted on the panel with dimensions of 1083 mm in width and 2140 mm in length, tilted at 30 degrees and exposed to a wind velocity of 10 m/s, with the scaling factors ranging from 0.1 to 1. The results of the findings in Figure 11 show the trends of the forces and coefficients for different scaling factors and indicate that as the scaling factor decreases and the panel size reduces, the drag and lift forces decrease significantly. This decrease may be attributed to the reduced surface area of the panel that was exposed to the wind. However, the results show that the corresponding coefficients,  $C_L$  and  $C_D$ , did not exhibit pronounced changes with varying panel size. These coefficients remained almost constant, indicating that they are not influenced by the panel scaling factor.

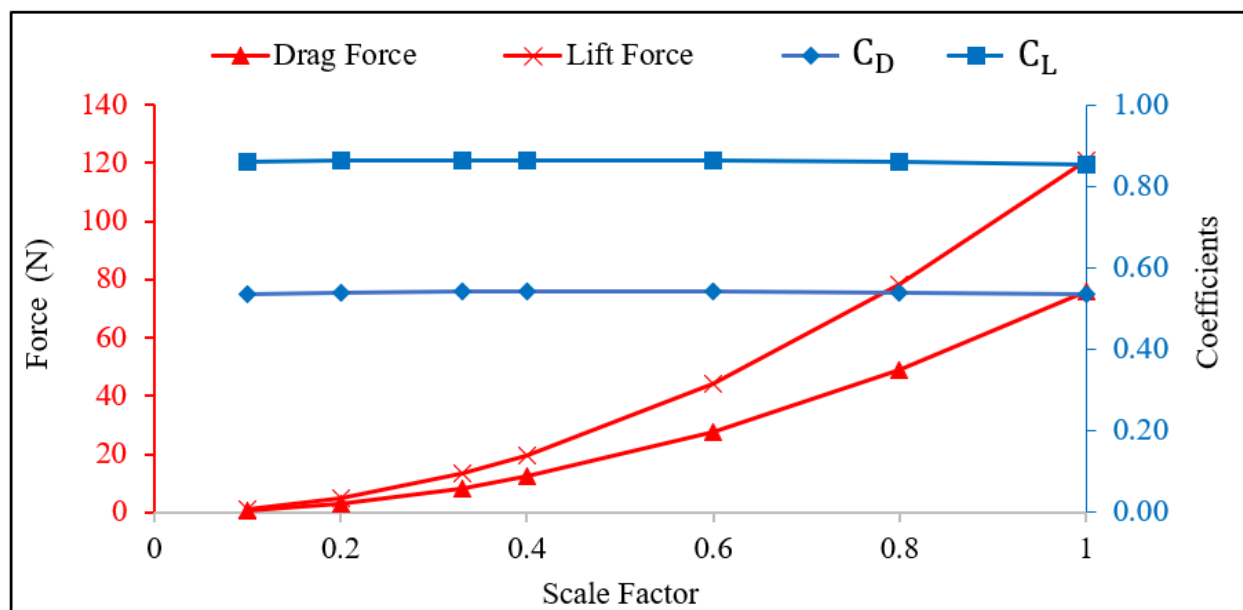


**Figure 11.** Drag and lift forces (in red) and corresponding coefficients,  $C_L$  and  $C_D$  (in blue), on the panel with different scaling factors at a 30-degree tilt angle and 10 m/s wind velocity.

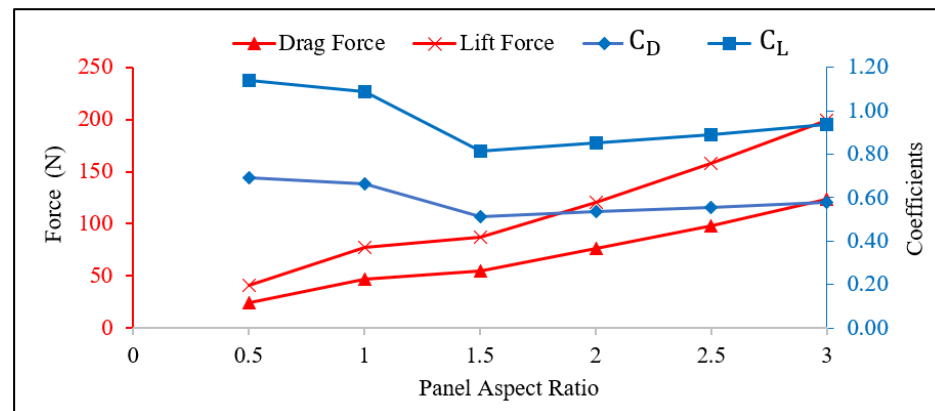
#### 4.4. Effects of Panel Aspect Ratio

Figure 12 presents the variation of drag and lift forces and their corresponding coefficients for panels with different aspect ratios between 0.5 and 3. These panels, tilted at 30 degrees and exposed to a wind velocity of 10 m/s, had a fixed width of 1083 mm, while the length ranged from 541 mm to 3249 mm. The findings from the results shown in Figure 12 reveal that panels with aspect ratios less than 1.5 exhibited higher values of  $C_L$  and  $C_D$  compared to panels with higher aspect ratios. For example, the values of  $C_L$  and  $C_D$  were 1.15 and 0.69, respectively, for the panel with an aspect ratio of 0.5. The results also show a steady increase in lift and drag coefficients with aspect ratios greater than 1.5, with the values of  $C_L$  and  $C_D$  ranging from 0.51–0.58 and 0.81–0.93, respectively. The observed differences in the values of  $C_L$  and  $C_D$  can be attributed to the influence of the panel aspect ratio on the aerodynamics of the panel.

#### 4.5. Aerodynamics of MSPT

A full-scale representation of the MSPT as illustrated in Figure 2 for the fabricated prototype, consisting of nine panels tilted at a constant angle of 30 degrees, was modelled following the previous simulation set-up outlined in Section 3. However, the symmetry boundary condition was not applied to the MSPT due to inherent asymmetries in the middle of the system. The dimensions of the MSPT, denoted as  $W_P$  and  $L_P$ , were 3612 mm and 6614 mm, respectively. Additionally, the dimensions of the corresponding simula-

tion domain, encompassing  $L_b$ ,  $L_f$ ,  $H$ , and  $B$ , were 15,500 mm, 7250 mm, 5418 mm, and 13,228 mm, respectively. Figure 13 provides a 3D representation of the computational domain including the boundary conditions of the CFD model for the MSPT.



**Figure 12.** Drag and lift forces (in red) and the corresponding coefficients,  $C_L$  and  $C_D$  (in blue), on the panel with different aspect ratios at a 30-degree tilt angle and 10 m/s wind velocity.

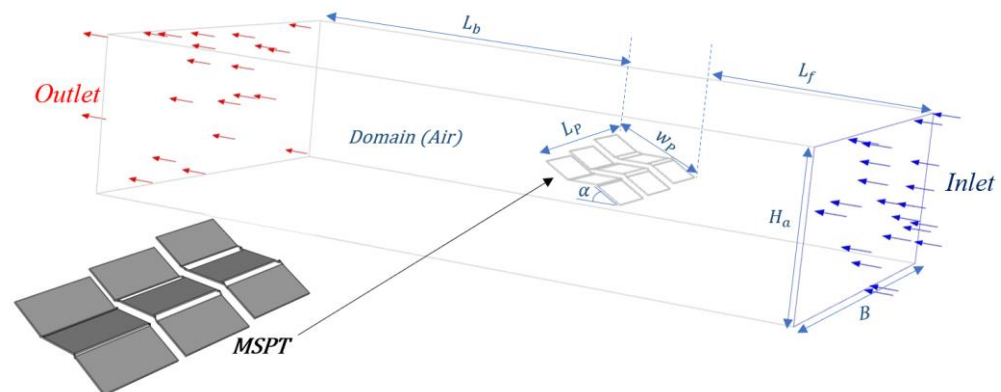


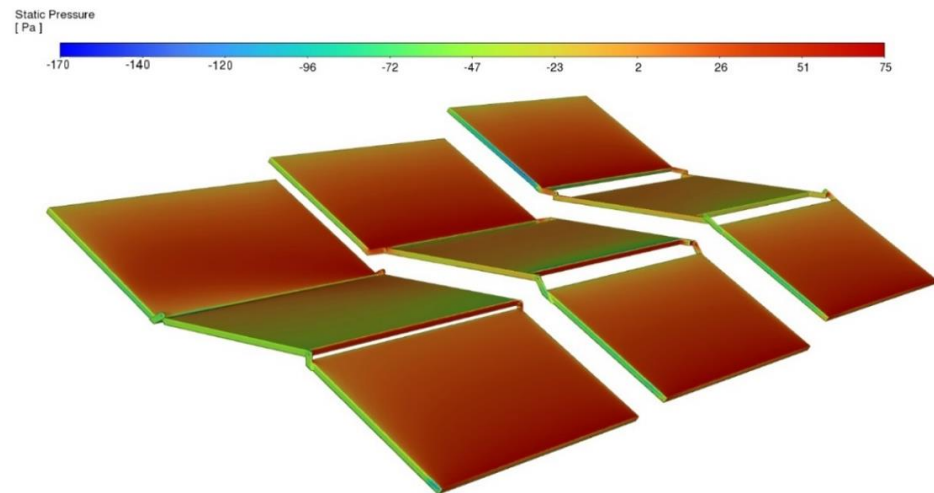
**Figure 13.** 3D view of the CFD model, showing the boundary conditions used to simulate the entire MSPT system (tilt angle,  $\alpha = 30$  degrees).

A wind velocity of 10 m/s was employed, as detailed in Section 3.2.1. However, to offer a more comprehensive understanding of the aerodynamic performance of the MSPT, more rigorous parametric studies were explored with wind velocities of 15 m/s and 20 m/s.

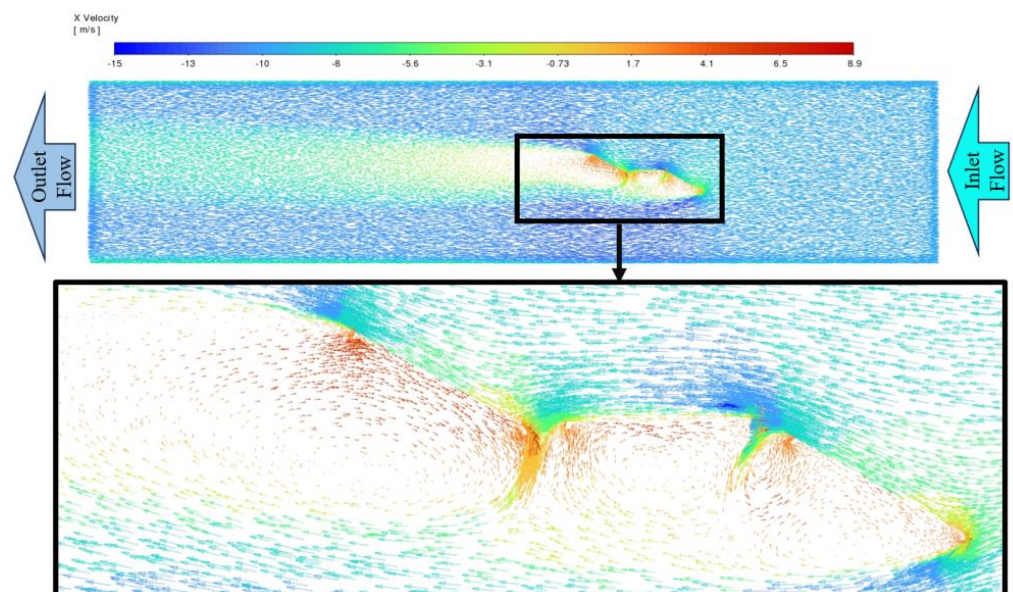
Figure 14 shows the static pressure contour of the panels in the entire MSPT (tilted at 30 degrees). The results in Figure 14 show that the bottom of the tilted panels experienced the maximum static pressure as the air flows over the entire MSPT, while the middle panels with no tilt angle exhibited minimum pressure.

Figure 15 shows the velocity vectors of flow in the x direction at the mid-section of the MSPT. As observed in Figure 15, flow separation led to a higher velocity magnitude, reaching up to 7.2 m/s compared to the inlet flow. Simultaneously, the back of the panels exhibited a suction flow with a maximum velocity of 6.2 m/s in the opposite direction to the inlet flow.

A comparison between Figures 7 and 15 reveals that the magnitude of the suction flow velocity around the MSPT was almost 62% higher compared to the individual panel. Also, comparing the results from Figures 6 and 14, the suction pressure occurring at the back of panels in MSPT was approximately 22% greater than that of a single panel. These observed differences may be attributed to the presence of gaps between panels in the MSPT, leading to an increase in turbulence.



**Figure 14.** Static pressure contour on the unfolded panels of the MSPT (tilted at 30 degrees).



**Figure 15.** Velocity vector of flow in the x direction (inlet to outlet) at the mid-section of the MSPT.

## 5. Discussion

A comparative analysis was undertaken to substantiate the exactness of the results obtained in the study and the implications. The analyses conducted entailed a juxtaposition of the results derived from the utilisation of the present technique with those documented in the existing scholarly works concerning solar photovoltaic (PV) panels [16,17]. The comparative evaluation involved a comprehensive review of both experimental data, as exemplified by Hoerner (1965) [31], and numerical investigations, as demonstrated by Georges et al. (2013) [23].

Figure 16 compares the values obtained for  $C_L$  and  $C_D$  for the current study with the values reported in the literature. As shown in Figure 16, there is a good agreement between the values of the lift and drag coefficients, which further demonstrates the robustness of the results obtained in this study. Figure 16 also shows that the coefficients exhibit nearly identical values for each tilt angle, indicating that the aerodynamic performance of the panels remains consistent regardless of the wind's direction relative to the panel orientation. This suggests that the aerodynamic coefficients are not affected by the facing direction of the wind (from the front side or back side), whether it is approaching from the front side or the back side, as also reported by Georges et al. (2013) [23]. This finding is important and

significant for the design and optimisation of the solar panel, particularly in Sub-Saharan Africa, where the wind direction can be difficult to predict.

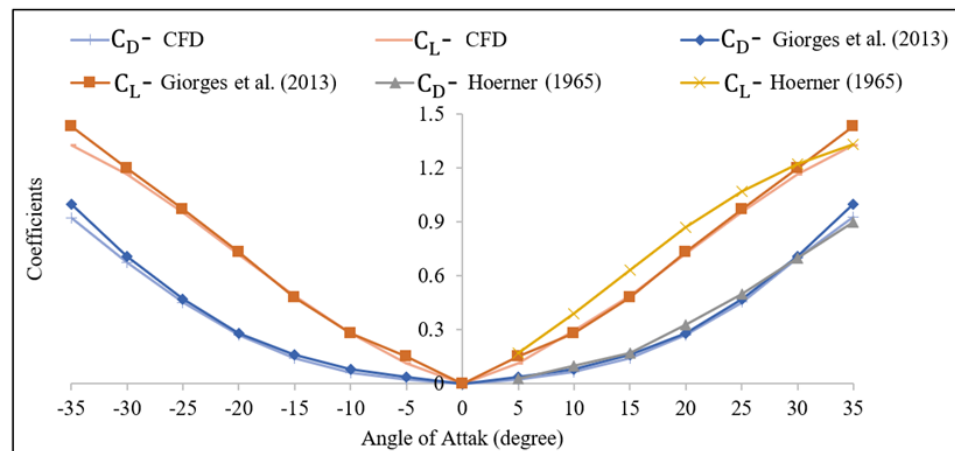


Figure 16.  $C_L$  and  $C_D$  for the unscaled panel (with a width of 699 mm and a length of 340 mm) at different tilt angles from the present study and the literature [23,31].

Figure 17 illustrates the drag and lift forces on the entire MSPT and the single panel under varying wind velocities. An increase in the drag and lift forces as the velocity increases from 10 m/s to 20 m/s for both the single panel and the entire MSPT is observed. For instances, the drag and lift forces on the entire MSPT under a wind velocity of 10 m/s were found to be 511 N and 941 N, respectively, whereas the drag and lift forces on the entire MSPT at a wind velocity of 20 m/s were found to be 2038 N and 3747 N, respectively. The data analysis indicates that the drag and lift forces at a wind velocity of 20 m/s are slightly more than four times greater than the corresponding forces at a wind velocity of 10 m/s.

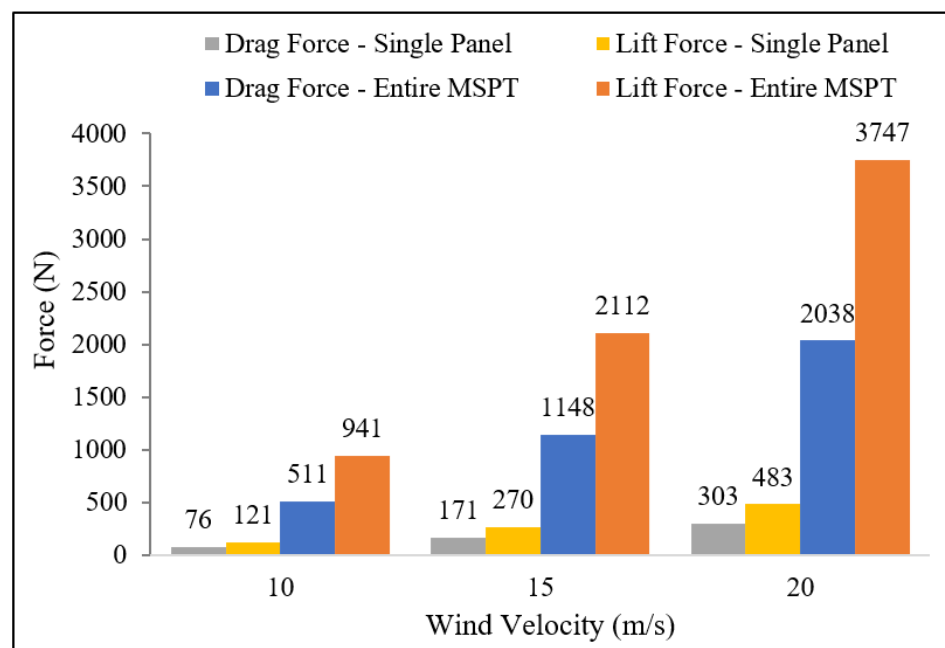


Figure 17. Drag and lift forces acting on the single panel and the entire MSPT system under different wind velocities.

Additionally, Figure 17 shows the drag and lift forces on the entire MSPT under different wind velocities to be approximately 6.7 and 7.8 times greater than the corresponding forces on a single panel with a 30-degree tilt angle used in the MSPT. Utilising

Equations (1) and (2) and taking the total area of the nine panels in the MSPT as 20.85 m<sup>2</sup>, and the air density to be 1.22 kg/m<sup>3</sup>, the drag and lift coefficients for the entire MSPT were determined to be 0.40 and 0.74, respectively, for all the three investigated wind velocities. It is important to note that these coefficients remained consistent and were not influenced by changes in wind velocity. As discussed in Section 4.1, it is noteworthy that for a single panel with a tilt angle of 30 degrees, the drag and lift coefficients were determined to be 0.53 and 0.85, respectively. This implies that simple superposition assumptions, such as considering nine or six times the forces on a single panel (accounting for the nine panels, with six tilted at 30 degrees), does not provide sufficient accuracy for determining the aerodynamic forces on the entire MSPT.

## 6. Conclusions

Mobile solar PV systems are becoming increasingly recognised as crucial solutions for clean and renewable energy, especially in off-grid areas. This study employed numerical and experimental techniques to scrutinise the aerodynamic characteristics of an innovatively designed MSPT system, featuring nine large solar PV panels.

The focus of this study was an average wind velocity of 10 m/s, reflective of Sub-Saharan Africa, specifically Nigeria's annual wind speeds. The investigation explored the impacts of wind velocity and tilt angles on drag and lift forces. The primary comparative parameters for aerodynamic analysis were the lift and drag coefficients ( $C_L$  and  $C_D$ ). Employing ANSYS-Fluent 2022/R2 software, the simulations for a single solar PV panel were validated through experimental tests on a 1:15 scaled-down model. Additionally, the study validated the numerical approach by comparing the results with documented cases of a solar PV panel found in the literature.

Moreover, this study explored the impact of several factors on the aerodynamics of solar PV panels. Primary considerations encompassed tilt angles and wind velocities. Furthermore, recognising gaps in the existing literature, the investigation was extended to the impact of scaling size and the aspect ratio of the panels on the aerodynamics and flow behaviour around the panels.

The results across all studied scenarios indicated that aerodynamic coefficients remained unaffected by wind direction, whether the wind approached the solar panel from the front or back side. The CFD analysis on a single full-size panel in the MSPT revealed a nonlinear increase in drag and lift forces with higher wind velocities. Scaling down the panels showed a significant decrease in forces due to reduced wind exposure, following a power-law relationship. However, lift and drag coefficients exhibited minimal changes with varying panel size. Panels with aspect ratios below 1.5 demonstrated higher  $C_L$  and  $C_D$  values compared to those with higher aspect ratios.

Examining the overall wind force on the entire MSPT accounted for combined wind flow and system geometry effects. The CFD results indicated increased turbulence caused by gaps between panels, leading to almost 62% higher suction flow velocity and 22% higher suction pressure compared to a single panel. Furthermore, drag and lift forces on the entire MSPT were approximately 6.7 and 7.8 times greater than those on a single panel with the same 30-degree tilt angle. The corresponding drag and lift coefficients for the entire MSPT were found to be 0.40 and 0.74, respectively, while for a single panel tilted at 30 degrees, the values of  $C_L$  and  $C_D$  were 0.53 and 0.85, respectively. It is clear from this study that simple superposition assumptions, considering the forces on a single panel, cannot accurately predict the aerodynamic forces on the entire MSPT. Therefore, a further aerodynamic investigation is found to be necessary to determine the wind effects on the entire system more accurately. Therefore, the author would like to recommend further aerodynamic investigations to precisely determine the wind effects on the entire system.

In conclusion, this study provided significant insights into the aerodynamic behaviour of mobile solar PV systems, facilitating a comprehensive understanding of their performance under diverse wind conditions. These findings would be vital for optimising the design and operation of such systems, ultimately enhancing their efficiency and reliability,

especially in Sub-Saharan Africa. The integration of CFD simulations and experimental validation contributed to the knowledge in the field, opening avenues for further advancements in mobile solar PV technology.

**Author Contributions:** Conceptualisation, A.E.M., F.T.-M. and D.S.A.; methodology, A.E.M. and D.S.A.; investigation, A.E.M. and D.S.A.; resources, A.E.M., D.S.A. and F.T.-M.; data curation, A.E.M., F.T.-M., D.S.A., N.N.E., J.W., D.N. and Z.M.; writing—original draft preparation, A.E.M., F.T.-M. and D.S.A.; writing—review and editing, A.E.M., F.T.-M., D.S.A., N.N.E., J.W., D.N. and Z.M.; visualisation, A.E.M., F.T.-M., D.S.A., N.N.E., J.W., D.N. and Z.M.; supervision, F.T.-M., D.S.A. and N.N.E.; project administration, F.T.-M. and D.S.A.; funding acquisition, F.T.-M. and D.S.A. All authors have read and agreed to the published version of the manuscript.

**Funding:** This work was funded by the INNOVATE UK project No: 833831 and partially supported by the ReACTIVE Too project that has received funding from the European Union’s Horizon 2020 Research, Innovation and Staff Exchange Programme under the Marie Skłodowska-Curie Action (Grant Agreement No. 871163).

**Data Availability Statement:** The data presented in this study are available on request from the corresponding author.

**Acknowledgments:** The authors would also like to acknowledge the support of Paul Bates and George Dye for building the sample for the test.

**Conflicts of Interest:** Author Dave Nwosu was employed by the company Nevadic Limited. Author Zackery Matthews was employed by the company DZP Technologies Limited. The remaining authors declare that the research was conducted in the absence of any commercial or financial relationships that could be construed as a potential conflict of interest.

## References

- Jacobson, M.Z.; Delucchi, M.A.; Bauer, Z.A.F.; Goodman, S.C.; Chapman, W.E.; Cameron, M.A.; Bozonnat, C.; Chobadi, L.; Clonts, H.A.; Enevoldsen, P.; et al. 100% Clean and Renewable Wind, Water, and Sunlight All-Sector Energy Roadmaps for 139 Countries of the World. *Joule* **2017**, *1*, 108–121. [[CrossRef](#)]
- Hu, M.; Song, X.; Bao, Z.; Liu, Z.; Wei, M.; Huang, Y. Evaluation of the Economic Potential of Photovoltaic Power Generation in Road Spaces. *Energies* **2022**, *15*, 6408. [[CrossRef](#)]
- Chomać-Pierzecka, E.; Kokieli, A.; Rogozińska-Mitrut, J.; Sobczak, A.; Soboń, D.; Stasiak, J. Analysis and Evaluation of the Photovoltaic Market in Poland and the Baltic States. *Energies* **2022**, *15*, 669. [[CrossRef](#)]
- Majd, A.E.; Tchienbou-Magaia, F.L.; Adebayo, D.; Bates, P.; Willetts, J.; Nwosu, D.; Stoeva, Z.; Ekere, N.N. Development of Affordable Mobile Solar Power Systems for Clean Energy Access. *WIT Trans. Ecol. Environ.* **2023**, *261*, 191–204.
- Yemenici, O.; Aksoy, M.O. An Experimental and Numerical Study of Wind Effects on a Ground-Mounted Solar Panel at Different Panel Tilt Angles and Wind Directions. *J. Wind Eng. Ind. Aerodyn.* **2021**, *213*, 104630. [[CrossRef](#)]
- Fardi Asrami, R.; Sohani, A.; Saedpanah, E.; Sayyaadi, H. Towards Achieving the Best Solution to Utilize Photovoltaic Solar Panels for Residential Buildings in Urban Areas. *Sustain. Cities Soc.* **2021**, *71*, 102968. [[CrossRef](#)]
- Talut, M.; Bahaj, A.S.; James, P. Solar Power Potential from Industrial Buildings and Impact on Electricity Supply in Bangladesh. *Energies* **2022**, *15*, 4037. [[CrossRef](#)]
- Peng, H.Y.; Dai, S.F.; Liu, H.J. Wind Loading Characteristics and Roof Zoning of Solar Arrays Mounted on Flat-Roofed Tall Buildings. *J. Build. Eng.* **2023**, *66*, 105823. [[CrossRef](#)]
- Stathopoulos, T.; Zisis, I.; Xypnitou, E. Local and Overall Wind Pressure and Force Coefficients for Solar Panels. *J. Wind Eng. Ind. Aerodyn.* **2014**, *125*, 195–206. [[CrossRef](#)]
- Su, K.-C.; Chung, P.-H.; Yang, R.-Y. Numerical Simulation of Wind Loads on an Offshore PV Panel: The Effect of Wave Angle. *J. Mech.* **2020**, *37*, 53–62. [[CrossRef](#)]
- You, J.; Lim, M.; You, K.; Lee, C. Wind Coefficient Distribution of Arranged Ground Photovoltaic Panels. *Sustainability* **2021**, *13*, 3944. [[CrossRef](#)]
- Browne, M.T.L.; Taylor, Z.J.; Li, S.; Gamble, S. A Wind Load Design Method for Ground-Mounted Multi-Row Solar Arrays Based on a Compilation of Wind Tunnel Experiments. *J. Wind Eng. Ind. Aerodyn.* **2020**, *205*, 104294. [[CrossRef](#)]
- International Code Council (ICC). *2021 International Building Code (IBC)*; International Code Council, INC: Country Club Hills, IL, USA, 2022.
- American Society of Civil Engineers *Minimum Design Loads and Associated Criteria for Buildings and Other Structures*; American Society of Civil Engineers: Reston, VA, USA, 2021; ISBN 9780784415788.
- Naeiji, A.; Raji, F.; Zisis, I. Wind Loads on Residential Scale Rooftop Photovoltaic Panels. *J. Wind Eng. Ind. Aerodyn.* **2017**, *168*, 228–246. [[CrossRef](#)]

16. Stenabaugh, S.E.; Iida, Y.; Kopp, G.A.; Karava, P. Wind Loads on Photovoltaic Arrays Mounted Parallel to Sloped Roofs on Low-Rise Buildings. *J. Wind Eng. Ind. Aerodyn.* **2015**, *139*, 16–26. [[CrossRef](#)]
17. Wang, Z.Y.; Plate, E.J.; Rau, M.; Keiser, R. Scale Effects in Wind Tunnel Modelling. *J. Wind Eng. Ind. Aerodyn.* **1996**, *61*, 113–130. [[CrossRef](#)]
18. Aly, A.M.; Bitsuamlak, G. Aerodynamics of Ground-Mounted Solar Panels: Test Model Scale Effects. *J. Wind Eng. Ind. Aerodyn.* **2013**, *123*, 250–260. [[CrossRef](#)]
19. Khan, A.K.; Shah, T.R.; Khosa, A.A.; Ali, H.M. Evaluation of Wind Load Effects on Solar Panel Support Frame: A Numerical Study. *Eng. Anal. Bound. Elem.* **2023**, *153*, 88–101. [[CrossRef](#)]
20. Wittwer, A.R.; Podestá, J.M.; Castro, H.G.; Mroginski, J.L.; Marighetti, J.O.; De Bortoli, M.E.; Paz, R.R.; Mateo, F. Wind Loading and Its Effects on Photovoltaic Modules: An Experimental–Computational Study to Assess the Stress on Structures. *Sol. Energy* **2022**, *240*, 315–328. [[CrossRef](#)]
21. Adaramola, M.S.; Oyewola, O.M. On Wind Speed Pattern and Energy Potential in Nigeria. *Energy Policy* **2011**, *39*, 2501–2506. [[CrossRef](#)]
22. Gesto. Nigeria re Projects: Solar and Wind Potential Evaluation. Available online: <https://gestoenergy.com/nigeria-re-projects-solar-and-wind-potential-evaluation> (accessed on 13 August 2023).
23. Georges, A.T.G.; Amador, G.J.; Caravati, K.; Goodman, J. Numerical Simulation of Aerodynamic Force on Solar Panels. In *Volume 6A: Energy, Proceedings of the ASME 2013 International Mechanical Engineering Congress and Exposition, San Diego, California, USA, 15–21 November 2013*; American Society of Mechanical Engineers: New York, NY, USA, 2013.
24. Versteeg, H.K.; Malalasekera, W. *An Introduction to Computational Fluid Dynamics: The Finite Volume Method*, 2nd ed.; Pearson Prentice Hall: Essex, UK, 2007.
25. Anderson, J.D. *Computational Fluid Dynamics: The Basics with Application*; McGraw-Hill: New York, NY, USA, 1995.
26. Chorin, A.J. Numerical Solution of the Navier-Stokes Equations. *Math. Comput.* **1968**, *22*, 745–762. [[CrossRef](#)]
27. ANSYS Inc. *ANSYS Fluent 2022 R2, Computer Software*; ANSYS Inc.: Canonsburg, PA, USA, 2022.
28. Fogaing, M.B.T.; Hemmati, A.; Lange, C.F.; Fleck, B.A. Performance of Turbulence Models in Simulating Wind Loads on Photovoltaics Modules. *Energies* **2019**, *12*, 3290. [[CrossRef](#)]
29. Wu, M.; Zhou, X. Study on Simulation of Wind Load Characteristics for Photovoltaic Generation Systems. *Vibroeng. Procedia* **2020**, *33*, 107–112. [[CrossRef](#)]
30. Su, K.-C.; Chung, K.-M.; Hsu, S.-T. Numerical Simulation of Wind Loads on Solar Panels. *Mod. Phys. Lett. B* **2018**, *32*, 1840009. [[CrossRef](#)]
31. Hoerner, S.F. *Fluid-Dynamic Drag*; Hoerner Fluid Dynamics: Bakersfield, CA, USA, 1965.

**Disclaimer/Publisher’s Note:** The statements, opinions and data contained in all publications are solely those of the individual author(s) and contributor(s) and not of MDPI and/or the editor(s). MDPI and/or the editor(s) disclaim responsibility for any injury to people or property resulting from any ideas, methods, instructions or products referred to in the content.